Nanoscale

COMMUNICATION

View Article Online
View Journal | View Issue

Cite this: *Nanoscale*, 2025, **17**, 17075

Received 12th June 2025,
Accepted 3rd July 2025

DOI: 10.1039/d5nr02511g

rsc.li/nanoscale

Electrochemical restructuring of H_2O_2 activated copper selenide for CO_2 reduction†

Wenjian Hu, [a,b] Deema Balalta, [c] Zhiyuan Chen,[b] Imran Abbas, [a] Jia Song, [b] Balázs Barhács, [d,e] Márton Guba, [d,e] Tibor Höltzl, [d,e,f] Francesco D'Acapito, [g] Thomas Altantzis, [h] Jan Vaes, [b] Sara Bals, [c] Didier Grandjean, *[a] Deepak Pant *[b,i] and Ewald Janssens *[a]

Copper chalcogenides such as $Cu_{2-x}Se$, acknowledged as efficient CO_2 reduction catalysts, do not represent the active phases but rather are precursors or pre-catalysts as they undergo significant transformations under reaction conditions. In this work we have tailored the initial structure of $Cu_{2-x}Se$ to steer structural evolution under catalytic conditions and facilitate the generation of the active phases. As-prepared $Cu_{2-x}Se$ nanowires were reconstructed through H_2O_2 and electrochemical treatments, yielding distinct pre-catalysts. Their electrochemical reduction was found to be an effective strategy to enhance the formation of active metallic Cu nanoparticles. Chemical pretreatment with H_2O_2 further accelerates this process by inducing a structural loosening and partial oxidation of the $Cu_{2-x}Se$ phase. Supported by *in situ* Raman spectroscopy, quasi-*in situ* X-ray diffraction, X-ray absorption fine structure spectroscopy and high-angle annular dark-field scanning transmission electron microscopy analysis, it is suggested that structural transformation is a common feature of many copper-based catalysts during CO_2 electroreduction. The as-prepared $Cu_{2-x}Se$ nanowires, with diameters of about 300 nm, exhibit a 23% methanol selectivity and a low CO_2 selectivity of only 4% at −1.4 V *versus* the reversible hydrogen electrode. In contrast, 50–90 nm Cu_2O cubes obtained after H_2O_2 oxidation and electro-activation treatments, also acting as pre-catalysts, have a CO selectivity up to 82%. Density functional theory computations demonstrate lower binding energy of reaction intermediates, including *CO, on metallic Cu (110) than on Cu_2Se (220), which may account for the enhanced CO production of the electro-activated catalyst. Our work sheds light on the dependence of the catalytic performance of copper selenide on its initial restructuration and provides guidance for the development of efficient and selective CO_2 conversion catalysts.

Introduction

The process of CO_2 electroreduction using Cu catalysts[1,2] has garnered tremendous attention, because Cu demonstrates remarkable activity for the production of high-valued products such as alcohols. However, obtaining a specific product with high selectivity remains a challenge.[2] Several strategies are being followed to improve the efficiency and selectivity of the electrochemical CO_2 reduction reaction (CO_2RR) on copper catalysts, such as morphology control,[3] surface modification,[4] oxide-derived copper,[5] single Cu atoms,[6] and alloying.[7] Alloying Cu with other metals can enhance the selectivity of CO_2RR toward different products by modulating the catalyst's electronic structure and thereby the adsorption of reaction intermediates.[8]

Similarly, combining copper with non-metallic elements to form copper chalcogenides, such as $Cu_{2-x}Se$, has gained attention.[9–11] The presence of selenium atoms modulates the electronic structure, in particular the Cu d-band center. This alters the adsorption behavior of reaction intermediates and thereby the catalyst's specificity and effectiveness. Recent studies on copper selenide catalysts demonstrated significant enhancements in CO_2 electroreduction towards methanol and

[a]*Quantum Solid-State Physics, Department of Physics and Astronomy, KU Leuven, Celestijnenlaan 200 D, 3001 Leuven, Belgium. E-mail: ewald.janssens@kuleuven.be, didier.grandjean@kuleuven.be*
[b]*Electrochemistry Excellence Centre, Materials & Chemistry Unit, Flemish Institute for Technological Research (VITO), Boeretang 200, 2400 Mol, Belgium. E-mail: deepak.pant@vito.be*
[c]*Electron Microscopy for Materials Science (EMAT), University of Antwerp, Groenenborgerlaan 171, 2020 Antwerp, Belgium*
[d]*Department of Inorganic and Analytical Chemistry, Budapest University of Technology and Economics, Szent Gellért tér 4, 1111 Budapest, Hungary*
[e]*Furukawa Electric Institute of Technology, Késmárk utca 28/A, 1158 Budapest, Hungary*
[f]*HUN-REN-BME Computation Driven Research Group, Budapest University of Technology and Economics, Szent Gellért tér 4, H-1111 Budapest, Hungary*
[g]*CNR-IOM-OGG c/o ESRF LISA CRG – The European Synchrotron, 71 Av. des Martyrs, 38000 Grenoble, France*
[h]*Applied Electrochemistry & Catalysis (ELCAT), University of Antwerp, Universiteitsplein 1, 2610 Wilrijk, Belgium*
[i]*Center for Advanced Process Technology for Urban Resource Recovery (CAPTURE), Frieda Saeysstraat 1, 9052 Zwijnaarde, Belgium*

† Electronic supplementary information (ESI) available. See DOI: https://doi.org/10.1039/d5nr02511g

ethanol.[11] Optimizing the composition and structure of copper selenide by potassium or vanadium doping,[12,13] or by creating selenium vacancies,[14,15] also has proven effective to increase its selectivity and efficiency for ethanol.

While excellent results were reported using copper chalcogenides for CO_2RR, the identification of the active states remain incomplete.[16–22] This is largely due to the structural reconstruction under CO_2RR conditions that occurs even in Cu-based catalysts with well-defined nanostructures.[23,24] In particular, most active sites on the surface of metal compounds experience irreversible reconstruction induced by electro-derived reduction or oxidation processes, which critically affects product selectivity.[25,26]

Recent *operando* and *in situ* method developments provide powerful non-destructive tools to probe the active sites and structural changes in Cu-based electrocatalysts under reaction conditions. Grazing incident X-ray diffraction reveals that CuO nanoplate catalysts are transformed into a mixture of metallic copper and Cu_2O after a single minute of electrochemical reduction at −0.6 V_{RHE}.[27] An *in situ* Raman study has shown that typical Cu_2O peaks (~620 cm^{-1}) disappear below −0.2 V_{RHE} *versus* the reversible hydrogen electrode (RHE),[5] indicating a reduction of surface Cu^+ to metallic Cu. Thermodynamically, CuO_x phases should be removed under CO_2RR conditions along with the active $Cu^{\delta+}$ species.[28] However, the underlying reason for the existence of dynamical $Cu^{\delta+}$ species remains to be uncovered.[29] More recently an *operando* analytical and four-dimensional electrochemical liquid-cell scanning transmission electron microscopy (STEM) investigation has shown that a Cu nanoparticle ensemble evolves into metallic Cu nanograins during electrolysis, before complete oxidation to single-crystal Cu_2O nanocubes following post-electrolysis air exposure.[2] Similarly, Yoon *et al.* demonstrated that CuI, formed *via* iodide pre-treatment, transforms into filament-like metallic Cu nanostructures under cathodic potentials in an iodide-free $KHCO_3$ electrolyte. When the applied bias was removed and the system returned to open circuit potential, partial re-oxidation occurred, resulting in the re-formation of Cu^+-based CuI and Cu_2O particles.[30] These studies enhance understanding about the intricate characteristics of active Cu sites for CO_2RR. It also triggers the question whether post-electrolysis complete oxidation to single-crystal Cu_2O nanocubes is a common phenomenon for Cu-based materials.

The electrolyte has a role in the restructuring behavior of copper-based catalysts during CO_2 electroreduction. In conventional aqueous electrolytes, Cu-based catalysts such as Cu_2O typically undergo rapid and complete reduction to metallic Cu^0 under CO_2 reduction potentials.[31] In contrast, intermediate oxidation states like Cu^+ can be stable in an ionic liquid, thus suppressing the reduction kinetics. Such stabilization effect has been reported in prior studies, where $Cu_{2-x}Se$ nanowires retained their structure in an ionic liquid electrolyte, even after CO_2 reduction,[32,33] although several studies have shown that some as-prepared catalysts are not the actual reactive species, but rather their precursors or pre-catalysts.[34] Modification of their initial structure may influence the formation and availability of the actual reactive species.

In this work, we investigate the restructuring process of $Cu_{2-x}Se$ with the aim to enhance understanding about the active sites and ultimately control the product selectivity. To this end, the restructuring of as prepared $Cu_{2-x}Se$ nanowires was induced through hydrogen peroxide (H_2O_2) chemical activation and electro-activation. The H_2O_2 pre-treatment facilitates oxidation and loosening of the $Cu_{2-x}Se$ framework, enhancing its susceptibility to electrochemical activation.[11] We utilize an ionic liquid electrolyte to stabilize Cu^+ intermediates and suppress reduction kinetics. By integrating *in situ* with quasi-*in situ* spectroscopic characterization, we demonstrate that $Cu_{2-x}Se$ dynamically restructures to highly active metallic Cu under CO_2RR conditions. Cu_2O monocrystals, ranging in size from 50 to 90 nm, obtained by the activation processes were also found to function as pre-catalysts rather than being the actual active species. While the as-prepared $Cu_{2-x}Se$ nanowires favour methanol production, the restructured Cu_2O monocrystals mixed with $Cu_{2-x}Se$ exhibit an 82% faradaic efficiency (FE) for CO at −1.4 V_{RHE}.

Results and discussion

Synthesis and characterization of $Cu_{2-x}Se$ pre-catalysts

$Cu_{2-x}Se$ catalysts were synthesized by a water evaporation-induced self-assembly method, applying the procedure described in ref. 35. Those as-prepared $Cu_{2-x}Se$ nanowires (AP-CuSe) were subsequently restructured using two distinct methodologies. As shown in Scheme 1, the first method entails direct electro-activation, where $Cu_{2-x}Se$ was directly exposed to reductive (−1.6 V_{RHE}) electrochemical conditions (EA-CuSe). The second method is a sequential approach, starting with a chemical oxidative activation using hydrogen peroxide for 2 minutes (CA-CuSe), followed by electro-activation (EA-CA-CuSe). This approach results in four distinct and reproducible materials and allows to assess the impact of an initial superficial oxidative chemical treatment on the electrochemical reconstruction of $Cu_{2-x}Se$ nanowires.

The four different materials were extensively characterized by electron microscopy. The Field Emission Scanning Electron Microscopy (FE-SEM) image of AP-CuSe presented in the ESI (Fig. S2a†), shows bundles of one-dimensional $Cu_{2-x}Se$ nano-

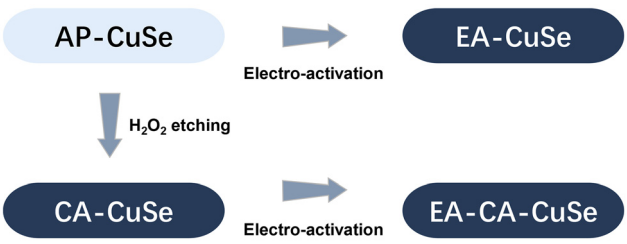

Scheme 1 Schematic overview of the relation between the four CuSe-based catalyst materials studied in this work.

wires with lengths of several micrometers and diameters of 100–500 nm. These 1D nanostructures have a relatively smooth surface. On the other hand, the CA-CuSe wires treated with H_2O_2 for varying durations (10 s, 2 min, and 10 min) have a rough, flocculent surface. Fig. S2b–d† show that their rough surface structure develops further upon longer H_2O_2 treatment. High Angle Annular Dark Field (HAADF) STEM, Energy Dispersive X-ray Spectroscopy (EDS) and Electron Energy Loss Spectroscopy (EELS) characterization provides deeper insights into the morphology, structure, and composition of the individual nanowires. Fig. 1a shows that the AP-CuSe nanowire bundles have a porous nature and are comprised of thin loosely-packed nanowires with few nanosheets located at their edges (Fig. S3a and S3b in the ESI†). EELS of the thin nanosheets confirms their mixed chemical composition of Cu and Se (Fig. S8a†). The interatomic distances measured from high resolution HAADF STEM images and the corresponding Fast Fourier Transform pattern (FFT) (Fig. 1e) are in agreement with the cubic structure (space group: $Fm\bar{3}m$) of $Cu_{2-x}Se$.[36]

The rough flocculent surface of CA-CuSe (Fig. 1b) consists of thin low-crystalline wrinkled sheets as highlighted by the high magnification HAADF STEM images (Fig. 1f). The thin outer surface is rich in copper and oxygen but depleted in selenium as observed in the EDS elemental mapping (Fig. 1i) and the atomic ratios in the line profile analysis along the nanowire cross section (Fig. 1j). These observations suggest that the hydrogen peroxide treatment has led to the formation of a thin superficial copper oxide layer.

Some of the basic nanowire morphology is retained after direct electrochemical reconstruction (EA-CuSe), as seen in HAADF STEM and SEM images (Fig. 1c, S3e, S3f, and S4†). However, the interior of the nanowire exhibits a significant degree of fragmentation into cube-like particles. High resolution HAADF STEM reveals its structural transformation into Cu_2O nanocubes (space group: $Pn\bar{3}m$)[37] and fragmented pieces of $Cu_{2-x}Se$, as confirmed by the interatomic distances (Fig. S5†) and the EDS elemental distribution maps (Fig. 1k and S6†).

Upon combination of chemical and electro-activation, EA-CA-CuSe (Fig. 1d, S3g, and S3h†), $Cu_{2-x}Se$ exposed to the ambient displays a structure similar to that of EA-CuSe but with further fragmentation of the nanowires into single crystalline Cu_2O nanocube aggregates, surrounded by small $Cu_{2-x}Se$ particles as shown in Fig. 1g and h and confirmed by the

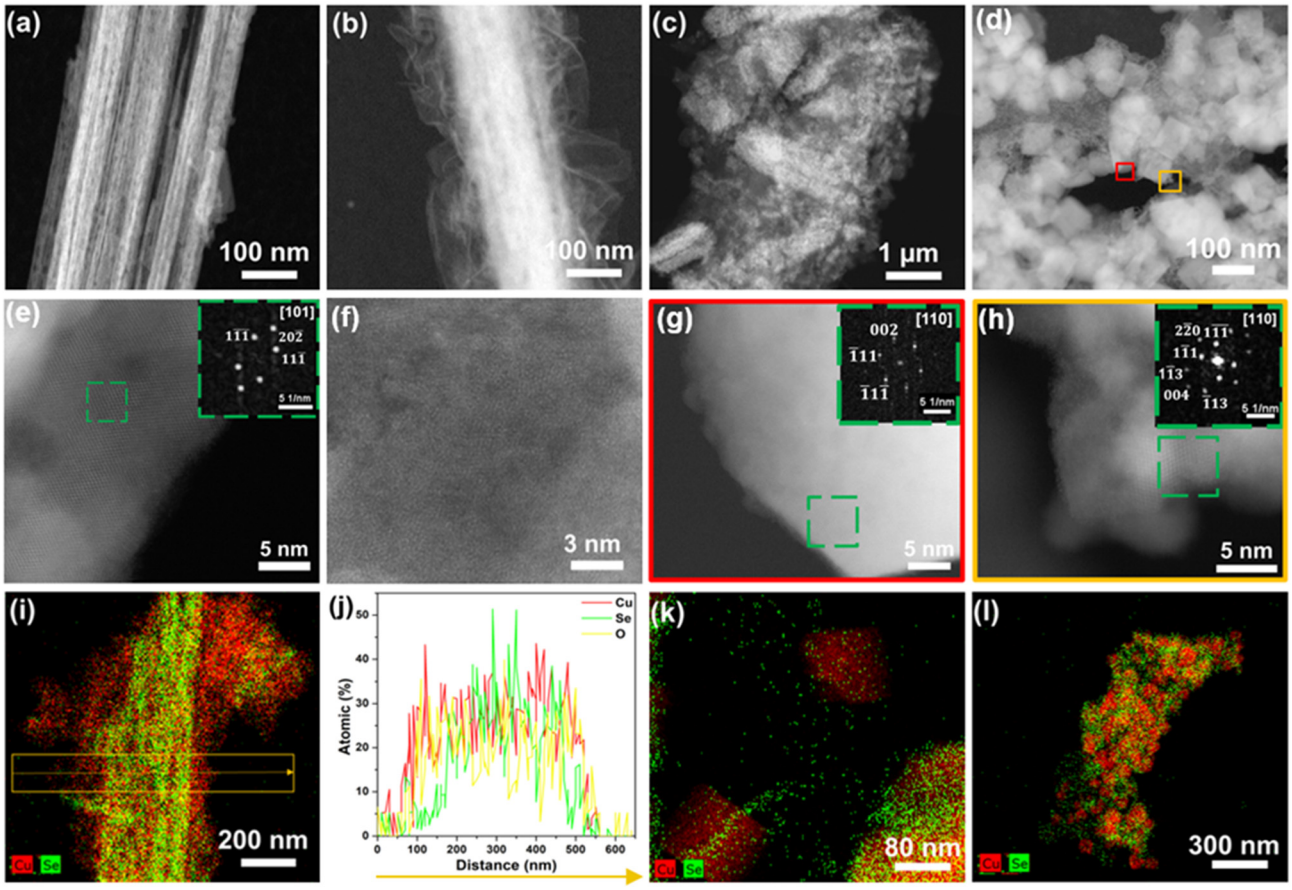

Fig. 1 HAADF-STEM images of (a and e) AP-CuSe, (b and f) CA-CuSe, (c) EA-CuSe, (d, g and h) EA-CA-CuSe. FFT pattern insets in (e, g and h) show the zone axis and the crystalline planes of the crystal structures in the green dashed squares. EDS elemental maps of (i) CA-CuSe, (k) EA-CuSe, and (l) EA-CA-CuSe. (j) Line scan along the cross-section of the CA-CuSe nanowire in (i), which shows that Cu is preferentially present at the surface.

corresponding FFT and the EELS analysis (Fig. S8b†). We note that the contrast variations in HAADF-STEM images arise mainly from differences in atomic number and local thickness, rather than from unequal beam penetration. The observed morphological heterogeneity, including wire-like, sheet-like, and blocky features, consistently appearing across different areas of each sample reflects the diversity of $Cu_{2-x}Se$ structures and their process-dependent restructuring. We conclude that the original $Cu_{2-x}Se$ nanowire structure has post electro-activation (both EA-CuSe and EA-CA-CuSe) transformed into 50–90 nm single-crystal Cu_2O nanocubes (cubic, $Pn\bar{3}m$) surrounded by $Cu_{2-x}Se$ nanoparticles. Analysis of the EDS maps in Fig. 1l and S7† give an atomic Cu : Se ratio close to 9 : 1 (Table S1 in the ESI†), supporting the transformation of CuSe into separate Cu- and Se-based phases, which are further characterized below.

The crystalline structure and composition of the bulk $Cu_{2-x}Se$-based samples were characterized by X-ray diffraction (XRD), summarized in Fig. 2a. XRD patterns of AP-CuSe and CA-CuSe show diffraction peaks at 31.4°, 36.4°, 52.4°, 62.4°, 77.3° and 85.5°, which are ascribed to the (111), (200), (220), (311), (400) and (331) crystal planes of $Cu_{1.71}Se$ (ICDD: 04-024-2132), respectively and no impurity peaks are detected. The relatively large width of the diffraction peaks confirms that the CuSe nanowire bundles are made up of thin nanofibers with diameters of less than 10 nm, in line with previous work.[38] Although CA-CuSe features the same diffraction pattern as AP-CuSe, all XRD peaks are notably shifted towards higher angles. Using Bragg's law, those shifts correspond to a lattice contraction of about 3%, which can be attributed to the migration of copper to the surface of the material, accompanied by the creation of Cu vacancies in the CuSe phase and the formation of a copper oxide phase. Similar shifts of the diffraction peaks of copper selenide, corresponding to lattice contraction, have been reported previously.[39] The formation of the copper oxide phase is confirmed by the emergence of a peak at 45°, associated with the (111) plane of CuO (ICDD: 04-006-4186). After electro-activation, all $Cu_{2-x}Se$ and CuO peaks disappeared, while both EA-CuSe and EA-CA-CuSe have narrow diffraction peaks at 49.8°, 73.1° and 88.6°, ascribed to the (200), (220), and (222) crystal planes of Cu_2O (ICDD: 00-005-0667). The absence of the Cu_2O (111) plane at 42.7° could indicate that crystal growth is restricted in this direction, with a preference for other growth orientations. Such suppression of the (111) plane and preferential growth along the (200) direction has been observed before in thin Cu_2O films.[40] The Cu_2O grain size in the EA-CA-CuSe sample, calculated using Scherrer's equation, is 90 nm, which agrees with the size of the Cu_2O cubic structures observed with STEM.

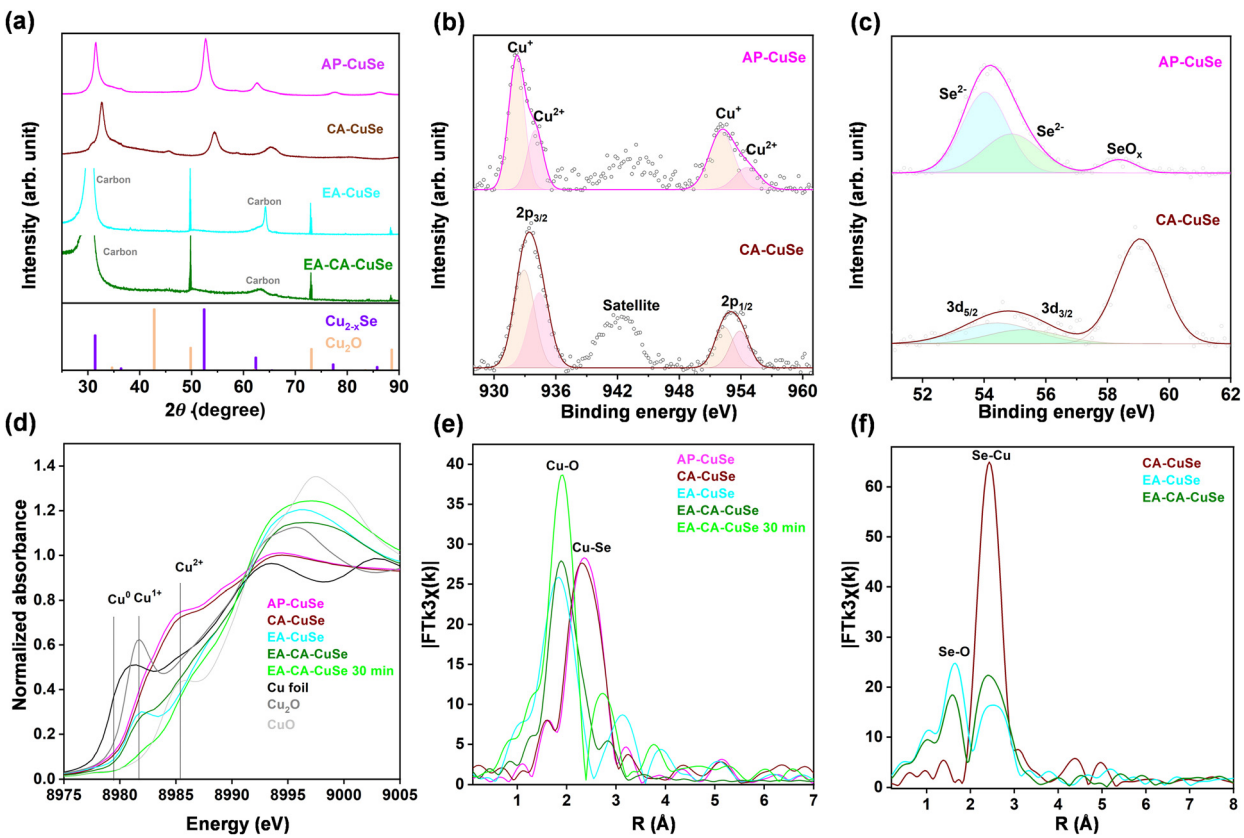

Fig. 2 (a) XRD spectra of the different $Cu_{2-x}Se$-based samples. XPS of AP-CuSe and CA-CuSe samples at the (b) Cu 2p and (c) Se 3d levels. (d) Cu K-edge XANES. Fourier Transforms of (e) Cu K-edge and (f) Se K-edge k^3-weighted EXAFS spectra.

The effect of H_2O_2 chemical activation on the surface was investigated by X-ray photoelectron spectroscopy (XPS), through comparison of Cu 2p (Fig. 2b), Se 3d (Fig. 2c), and O 1s (Fig. S9†) valence states of AP-CuSe and CA-CuSe. In the high-resolution Cu 2p spectra of the AP-CuSe, Cu $2p_{1/2}$ and $2p_{3/2}$ peaks at 952.2 and 932.1 eV are attributed to Cu^+ and the shoulders at 954.3 and 934.1 eV to Cu^{2+}. In CA-CuSe, all Cu 2p peaks shift to higher binding energies (maxima at 952.4 and 933.0 eV), indicating a general increase in the Cu oxidation state. After H_2O_2 treatment, the Cu^{2+} to Cu^+ ratio increases from 0.38 to 0.90, in line with the presence of a CuO phase as observed in the CA-CuSe XRD spectra. The O 1s spectrum of the AP-CuSe nano wires has a Cu–O peak at 530.1 eV and that of CA-CuSe can be deconvoluted in two peaks at approximately 529.4 and 531.3 eV, which can be attributed to Cu–O and Cu–OH, respectively. The copper hydroxide likely originates from the interaction between the catalyst and the aqueous solution. The deconvoluted AP-CuSe Se 3d peaks at 54.0 and 55.0 eV correspond to Se^{2-} $3d_{5/2}$ and $3d_{3/2}$. Another peak located at 58.3 eV is assigned to SeO_x, which is likely caused by oxidation of the samples in air. In CA-CuSe, the shift of the Se $3d_{5/2}$ and $3d_{3/2}$ peaks (54.3 and 55.4 eV) to higher energies, implies an increase in the Se oxidation state. The SeO_x peak is now at 59.0 eV and much more intense, which is due to the oxidizing H_2O_2 treatment.

The Raman spectrum of AP-CuSe (Fig. S10†) shows a peak at 259 cm^{-1}, which can be assigned to a Se–Se vibrational mode in copper selenide.[41,42] The absence of other peaks confirms the formation of a single $Cu_{2-x}Se$ phase. The CA-CuSe sample has an additional peak at 241 cm^{-1} that may be associated with intrinsic host lattice defects.[43] These defects could arise from superficial oxygen doping in $Cu_{2-x}Se$ or the formation of SeO bonds.[44] This further suggests that Se on the surface of the nanowires is oxidized following H_2O_2 treatment.

X-ray absorption near-edge structure (XANES) and extended X-ray absorption fine structure (EXAFS) spectra, measured on ambient-exposed samples at Cu and Se K-edges, allow to further investigate the electronic and structural properties of the CuSe catalysts before and after their activation. XANES spectra at Cu and Se K-edges are presented in Fig. 2d and Fig. S11,† respectively. XANES at Cu K-edge shows that AP-CuSe and CA-CuSe feature similar profiles. The significant structural and chemical transformation after electro-activation (EA-CuSe and EA-CA-CuSe), results in a shift of the edge position towards higher energy as well as the increase of the white line intensity. The characteristic profile of $Cu_{2-x}Se$ seen for AP-CuSe and CA-CuSe, transforms into profiles resembling a mixture of Cu_2O and CuO after electro-activation. The pre-edge peak corresponding to the 1s → 4p transition in Cu_2O that appears at approximately 8981.7 eV in EA-CuSe indicates that this sample contains a significant fraction of Cu_2O, while EA-CA-CuSe mainly consists of Cu^{2+} oxide whose fraction further increases when the latter treatment was prolonged to 30 min. The absence of the pre-edge located at around 8985.4 eV corresponding to the 1s → 4p transition in CuO, suggests that amorphous CuO combined with a hydroxide-like phase has formed in the EA-CA-CuSe sample. This is in line with the Se K-edge XANES that also exhibits two very distinct profiles for CA-CuSe on the one hand and EA-CuSe and EA-CA-CuSe on the other hand. The blue shift in energy and the increase of the white-line feature both indicate a significant oxidation of the Se phase following the electro-activation. XANES at both edges confirms the electro-activated transformation of a significant fraction of the original copper selenide phase into copper and selenium oxides.

Fourier transforms (FTs) before phase correction of k^3 weighted EXAFS at the Cu (Fig. 2e and S12†) and Se K-edges (Fig. 2f and S13) further confirm the drastic transformation of $Cu_{2-x}Se$, by segregation of copper and selenium atoms after electro-activation that forms large fractions of separate oxide phases after the samples are exposed to the ambient. The main peak at around 2.3 Å in FT at Cu K-edges of AP-CuSe and CA-CuSe was fitted by 2.6 and 2.8 Se at 2.395 Å, corresponding to the $Cu_{2-x}Se$ phase, while the shoulder at 1.7 Å was fitted by contributions of 0.8 and 1.0 O at 1.92 and 1.93 Å, respectively, corresponding to a mixture of Cu_2O, CuO and possibly Cu $(OH)_2$ (Table S2†). Using the copper oxygen coordination in Cu_2O (2 O at 1.85 Å) and CuO (4 O at 1.95 Å) as references, it is found that AP-CuSe and CA-CuSe consist of *ca.* 26% and 32% of oxide/hydroxide, respectively, while the rest of the samples remain in the Cu_{2-x} Se phase. Se K-edge analysis (Table S3†) confirms that CA-CuSe primarily consists of $Cu_{2-x}Se$, as indicated by two main FT peaks, which are fitted with 0.24 O at 1.66 Å and 5.1 Se at 2.41 Å, respectively. This composition includes a minor fraction, approximately 8% (0.24/3), of SeO_2, in which Se is coordinated with three O atoms.

Electro-activation of the AP-CuSe and CA-CuSe samples further transforms the CuSe phase into pure Cu and Se oxides as confirmed by the fits of the Cu K-edge EXAFS, highlighting a sharp increase of the O shells coordination to 2.1 and 2.5 atoms in EA-CuSe and EA-CA-CuSe samples and up to 3.7 O when the electro-activation is prolonged. The concomitant reduction of the Se shell coordination down to 2.0 in EA-CuSe and EA-CA-CuSe and 0.6 after 30 min of EA-CA-CuSe electro-activation is consistent with the segregation of $Cu_{2-x}Se$ into separate Cu and Se oxides. EA-CuSe and EA-CA-CuSe have similar fractions of copper oxide/hydroxide; 62% and 68%, respectively, which increases up to 92% after prolonged electro-activation of EA-CA-CuSe. Remarkably, a significant fraction of 31% of Cu_2O is still present in EA-CuSe, despite its exposure to the ambient. In the latter sample, the original $Cu_{2-x}Se$ cubic phase has been entirely transformed as even the tiny remaining part of copper selenide corresponds to the copper-poor CuSe hexagonal phase, characterized by shorter Cu–Se distances of 2.29 Å.[38] These results are in line with the analysis of Se K-edge EXAFS that highlights the presence of *ca.* 50% of SeO_2 (1.5–1.6 O at 1.66 Å), complemented by a mixture of $Cu_{2-x}Se$ (2.1–2.2 Se at 2.39–2.40 Å) and CuSe (1.0–0.9 Se at 2.19 Å) phases in EA-CuSe and EA-CA-CuSe.

The EXAFS results demonstrate, in good agreement with those obtained with the other characterization techniques, that the chemical and electrochemical treatments of $Cu_{2-x}Se$

nanowires produce highly distinctive materials through various surface reconstruction processes. Chemical activation of as-prepared samples induces the formation of a thin mostly amorphous copper oxide/hydroxide layer at the surface of the Cu_{2-x} Se nanowires, while the electro-activation transforms the material for a large part into SeO_2 (50% of Se) and copper oxide/hydroxide (62% of Cu) including up to 31% of Cu_2O in the form of single-crystal Cu_2O cubes (cubic, $Pn\bar{3}m$)[32] with 50 to 90 nm sizes. These cubes are surrounded by smaller particulates consisting of the remainder of the original $Cu_{2-x}Se$ as well as a copper-poor CuSe phase. Combined CA and EA treatment further completes the copper/selenium segregation (mixture of 92% of CuO_x and 8% Cu-poor CuSe) when the EA treatment is prolonged to 30 min.

Electrochemical CO_2RR performance

The electrochemical CO_2RR performance was investigated in an ionic liquid, namely 1-butyl-3-methylimidazolium tetrafluoroborate/acetonitrile/water electrolyte ([Bmim]PF_4-CH_3CN-H_2O), which enhances CO_2 solubility compared to aqueous solution. The different CuSe catalysts were dispersed in a Nafion-acetone solution and drop-cast onto Toray carbon paper (TGP-H-60), which served as the gas diffusion layer and working electrode (see SEM images in Fig. S14†). All electrochemical measurements were conducted in a two-compartment H-type cell separated by a Nafion 117 membrane.

As reference, polycrystalline Cu foil was tested under identical conditions at −1.4 V_{RHE} (Fig. S15†). The Cu foil reference exhibited a current density of around −2 mA cm^{-2} and produced 89.3% H_2, 8.1% HCOOH, and only 1.5% CO, indicating a modest CO_2 reduction activity in the ionic liquid electrolyte. In contrast, AP-CuSe treated for 2 minutes with H_2O_2 exhibited a relatively high current density in the Linear Sweep Voltammetry (LSV) measurements after achieving material stabilization (see Fig. S16 in the ESI†), making it a suitable candidate for further study. Current densities of the as-prepared and activated CuSe materials ranged from 1 to 36 mA cm^{-2} depending on the applied potentials. Chronoamperometry measurements of the four samples at different potentials shows that the activity of CA-CuSe decreases over time (Fig. S17†), which may be due to a rapid transformation of this catalyst under CO_2RR conditions. It is worth noting that at potentials of −1.2 V_{RHE} and lower, the current densities of EA-CA-CuSe and EA-CuSe samples increase over time, which may be attributed to a higher conductivity caused by the formation of metallic Cu at the surface.

The current density increases with the applied potential and is peaking for EA-CA-CuSe (36.7 mA cm^{-2} at −1.5 V_{RHE}), which is 9.7 and 4.3 times that of AP-CuSe (3.8 mA cm^{-2}) and CA-CuSe (8.4 mA cm^{-2}), respectively. EA-CA-CuSe exhibits also the highest partial current density for CO (Fig. 3a). Fig. 3b shows the FE of CH_3OH over the four catalysts, while Fig. 3c gives the FE of all products. AP-CuSe exhibits the highest selectivity towards methanol production, with values exceeding 22% in the −1.3 to −1.5 V_{RHE} potential range, while EA-CA-CuSe and CA-CuSe reach a maximum for methanol at −1.2 V_{RHE}, with values of 9.1% and 11.1%, respectively. The higher methanol selectivity of AP-CuSe indicates that untreated $Cu_{2-x}Se$ nanowires favour methanol production. On the other hand, EA-CA-CuSe yields the highest CO selectivity in a wide potential window with a maximum FE_{CO} of 82.1% ± 2.0% at −1.4 V_{RHE}.

Structure–reactivity relationship

To gain insight into the $Cu_{2-x}Se$ reconstruction mechanism and the reaction pathways under CO_2RR conditions, quasi *in situ* XRD patterns of the EA-CA pre-catalyst were measured immediately after electro-activation (Fig. 4a). The broad shoulder visible around 50.6° corresponds to the (111) plane of metallic copper, while the peak at 49.5° can be assigned to the (200) plane of Cu_2O (Cu^{1+}), confirming the reduction and segregation of Cu^{2+} from the original $Cu_{2-x}Se$ phase into Se-free reduced Cu phases. This provides strong evidence for the existence of Cu nanoparticles in the reduced phase. According

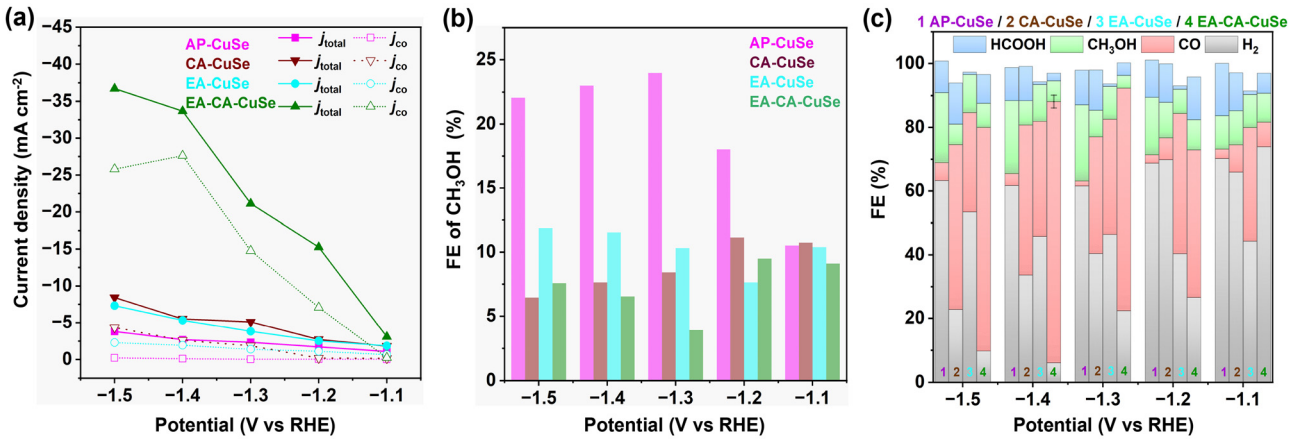

Fig. 3 Variation with the applied potential of (a) total current density and CO partial current density, (b) FE of CH_3OH and (c) FE of all products for AP-CuSe, CA-CuSe, EA-CuSe, and EA-CA-CuSe. The error bar on FE_{CO} for EA-CA-CuSe at −1.4 VRHE is the standard deviation of triplicate measurements. For other samples and bias voltages only single measurements were performed.

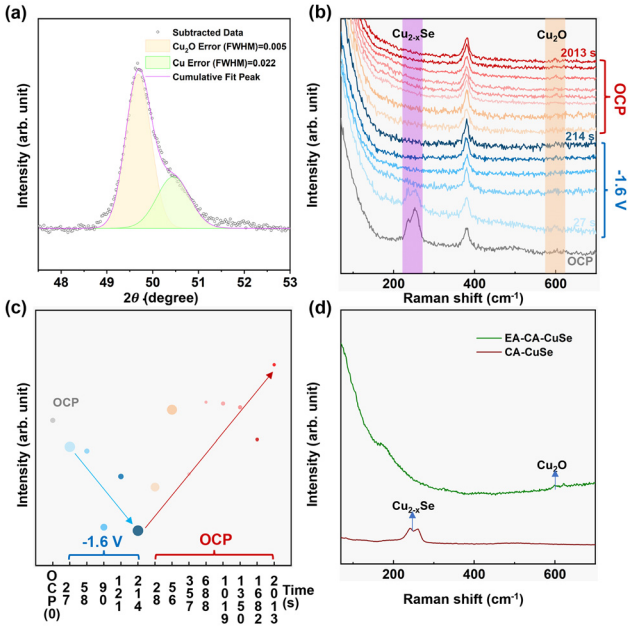

Fig. 4 EA-CA-CuSe (a) Quasi *in situ* XRD spectra. (b) In situ Raman spectra and (c) intensity of the Raman peak at 600 cm^{-1} in (b) as a function of the time during which −1.6 V_{RHE} is applied (blue symbols) or at OCP (red symbols). The size of the symbol represents the error bar. (d) Ex situ Raman spectra of CA-CuSe and EA-CA-CuSe.

to Scherrer's equation, the Cu_2O nanocrystallites formed after electrochemical activation exhibited an average size of approximately 14.3 ± 0.3 nm, representing a 20% increase compared to the metallic copper nanoparticles (11.9 ± 0.5 nm). This measured size increase corresponds well with theoretical value of 18%, indicating that Cu_2O likely forms through the oxidation of these metallic Cu nanoparticles.

The presence of Cu metal nanocrystallites under electroactivation conditions is further supported by *operando* and *ex situ* Raman spectra recorded for EA-CA-CuSe under −1.6 V_{RHE} (Fig. 4b and d) that shows a drastic reduction of the Cu–Se bond signal with time, indicating degradation of the $Cu_{2-x}Se$ phase and the build-up of pure metallic copper. The metallic phase is re-oxidized to Cu^{1+} as soon as the potential is returned to open circuit potential (OCP) as indicated by the increase of the Cu_2O signal in line with the results of the quasi *in situ* XRD analysis. Under the very negative potential, Cu is thus reduced and segregates from the original $Cu_{2-x}Se$ phase into metallic copper nanoparticles, while Se-rich copper selenide and pure Se oxide phases are formed. More specifically, the intensity of the Raman peak of CA-CuSe decreases rapidly once −1.6 V_{RHE} is applied and disappears after 1 minute (Fig. 4c).

XRD and STEM analyses conducted after exposure to ambient conditions reveal that the Cu_2O phase in the electroactivated material appears as large (50–90 nm) single-crystal cubes in EA and EA-CA-CuSe. This suggests that their formation results from the migration and agglomeration of numerous smaller nanoparticles, specifically 11.9 nm metallic Cu and/or 14.3 nm Cu_2O. Such agglomeration has been reported earlier in similar nanoparticle systems.[45,46] Additionally, surface oxidation of remaining metallic Cu could further contribute to gradual particle growth, even at OCP, driven by the residual oxidative species in solution.[47]

A recent *operando* STEM work hypothesized that catalytically active metallic copper nanograins form through the agglomeration of smaller Cu metal nanoparticles upon negative potentials.[2] The grain boundaries between the Cu nanoparticles serve as active sites for the formation of C_1 and C_2 products from CO_2RR. The porous structure and high reactivity of these nanograins would explain their fast transformation into Cu_2O cubes upon exposure to the ambient. Since the transformation of nanosized Cu into larger ordered Cu_2O nanocubes following exposure to ambient conditions is structurally irreversible, we hypothesize that transient Cu metal nanograins formed under CO_2RR activation—due to the segregation of Cu from the $Cu_{2-x}Se$ phase—serve as the active sites responsible for the enhanced methanol selectivity in the AP-CuSe catalyst. Moreover, in this study 11.9 nm Cu metal nanoparticles are expected to produce mostly C_1 products,[2] which is in line with the current results.

According to the characterization results from quasi-XRD and *operando* Raman spectroscopy, the high CO selectivity of EA-CA-CuSe may originate from the reduction of the large Cu_2O nanocubes formed by electro-activation.

Under CO_2RR conditions, these nanocubes form metallic surfaces that favor CO production. This observation aligns with documented research,[48] which describes the Cu_2O nanocubes undergo a multi-step reconstruction, developing rough surfaces, transitioning into hollow shells, and aggregating into mixed Cu/Cu oxide nanoparticles. It has been shown that Cu_2O nanocubes with sizes around 80 nm—comparable to the sizes observed in this study—achieve higher CO selectivity than larger particles, such as 170 nm and 390 nm cubes, supporting the importance of the particle size in optimizing CO formation.[49]

Upon treatment and exposure to the ambient, all samples contain a significant amount of copper oxide, highlighting $Cu_{2-x}Se$ degradation and the various degrees of segregation of Cu and Se phases into pure CuO_x and SeO_2 with a remaining small $Cu_{2-x}Se$ fraction.

AP-CuSe that comprises 13% Cu_2O and 13% CuO and 74% of $Cu_{2-x}Se$, exhibits methanol and CO selectivities of 23% and 4%, respectively at −1.4 V_{RHE}. Upon oxidation with H_2O_2, CA-CuSe is obtained, which contains 14% Cu_2O, 18% CuO and 68% of $Cu_{2-x}Se$ demonstrates a significant shift in product selectivity towards CO (FE_{CO} of 47%). The electrochemically activated EA-CuSe, with a much higher oxide content (68% Cu_xO), yields a CO selectivity of 36% at −1.4 V_{RHE}. Remarkably, the fourth material, EA-CA-CuSe, which underwent both peroxide oxidation and electro-activation, increasing the Cu_xO content to 92%, achieves the highest CO selectivity of 82% at the same potential. Across all derivatives, the selectivity for methanol decreased after any activation treatment of the original $Cu_{2-x}Se$, accompanied by a shift in catalytic behaviour favouring CO production.

Density functional theory calculations

To enhance our insight in the CO_2RR selectivity of the different $Cu_{2-x}Se$-derived catalyst materials, density functional theory calculations were performed on two model systems: Cu_2Se (220) and Cu (110), whose starting structures were based on ref. 11 and 50, respectively. The selection of the Cu (110) surface is driven by its previously reported high activity in CO_2 reduction[51] and its efficient C–O splitting capabilities,[52] which are relevant for CO formation. Both the Cu (110) and the Cu_2Se (220) structures were reoptimized by keeping the positions of the bottom atomic layer fixed, a commonly used method for slab models. Reaction free energies were calculated at −1 V and without voltage applied. More details of the computational methodology are provided in the ESI.† The Cu_2Se (220) slab is a proxy for the AP-CuSe sample because of its intense (220) diffraction peak (Fig. 2a) and the Cu (110) slab is a proxy for the reduced electro-activated catalysts (EA-CuSe and EA-CA-CuSe) under reaction conditions. Structural relaxation of the models with a fixed bottom layer indicated that Cu (110) underwent relatively small geometrical changes, while the surface atoms of Cu_2Se (220) significantly reorganized. This, combined with the known preference of the material for non-stoichiometric compositions, is characteristic of its structural flexibility that may lead to significant instability under reaction.

The computed reaction paths are consistent with those presented in literature.[11,50] The CO_2 reduction pathways towards CO and methanol under an applied bias of −1 V_{RHE} are presented in Fig. 5. In the applied computational hydrogen electrode model,[53] the effect of the cell voltage is taken into account after the quantum chemical computations. It downshifts the free energy, proportionally to the number of electrons needed to reach each intermediate. Methanol, which is the thermodynamically favoured product for both catalysts without applied cell voltage (Fig. S18 and S19†), is even more favoured at −1 V_{RHE}. CO desorption is endergonic, but CO hydrogenation is exergonic due to the applied voltage, making methanol formation thermodynamically more favoured. However, the selectivity towards different products on each catalyst is influenced strongly by the reaction kinetics. It has been shown that the CO binding energy is an important descriptor for the product selectivity.[54]

A notable difference between the computed reaction paths of the two model catalysts is the free energy change for CO desorption. On the Cu (110) surface, the desorption free energy is 1.0 eV, compared 1.5 eV for the Cu_2Se (220) surface (in computational hydrogen electrode the desorption free energy is independent of the applied bias). This can be attributed to the presence of less stable intermediates (except IN5) on the pure copper surface. Since CO desorption is irreversible, the easier desorption observed on the Cu surface implies a higher CO formation rate, consistent with the experimental results on both EA-Cu and EA-CA-CuSe.

However, it is important to note that oxide-derived copper possesses a highly complex structure. In fact, the catalysts studied here are chemically complex systems, and the simple models do not explain the non-monotonous potential-dependence of the product ratios shown in Fig. 3. Nevertheless, these simplified models allow for a qualitative assessment of the impact of distinct local chemical environments on CO binding and product selectivity. In this sense, the DFT results support the experimental observation that CO formation is favored on Cu-rich surfaces. Detailed reaction mechanism studies that lead to different products are currently the subject of intensive research. On the other hand, we noted that the detailed structure of our model system has a minimal impact on the energetics of the reaction, suggesting that the primary factor influencing the reaction is the local chemical environment at the reaction site, and the main factor to qualitatively understand the reactivity is the difference of the CO binding free-energies on the Cu (110) and Cu_2Se (220).

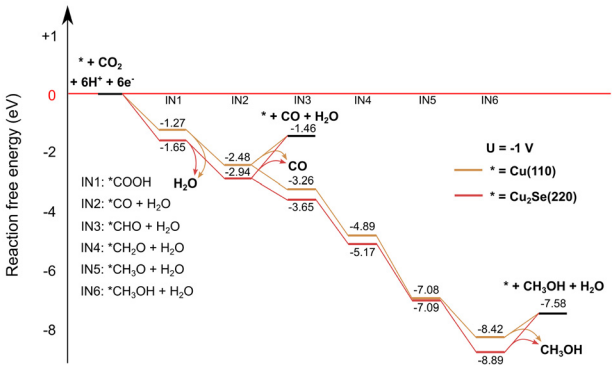

Fig. 5 Computed reaction CO_2RR pathways on Cu_2Se (220) and Cu (110) slab models to CO and methanol with an applied cell voltage of −1 V.

Conclusions

We showed that $Cu_{2-x}Se$, which is undergoing major restructuring under CO_2RR conditions, behaves rather as a pre-catalyst and developed a facile reconstruction strategy to transform it into active phases with tailored selectivity. Without H_2O_2 pre-treatment, direct *in situ* electroreduction of $Cu_{2-x}Se$ nanowires produces a small amount of metallic Cu nanoparticles, which reoxidize into Cu_2O nanocubes upon returning to open circuit, yielding a mixture of $Cu_{2-x}Se$ nanowires and Cu_2O cubes. In contrast, H_2O_2 pretreatment causes significant surface oxidation and nanowire fragmentation, destabilizing the as prepared material and resulting in the creation of metallic Cu nanoparticles during electroreduction. Those are largely converted to Cu_2O nanocubes after reaction. The resulting catalyst material consists mainly of Cu_2O nanocubes and residual $Cu_{2-x}Se$ nanoparticles, while the nanowire morphology is nearly lost. *In situ* and *ex situ* characterizations confirm that dynamic restructuring of $Cu_{2-x}Se$ involves Cu segregation from the selenide matrix.

A clear structure–selectivity relationship of copper-based catalysts was found. The as-prepared $Cu_{2-x}Se$ (AP-CuSe), which

dynamically transforms into Cu nanograins during CO_2RR, exhibits 23% methanol selectivity at −1.4 V_{RHE}. In contrast, the H_2O_2-etched and electrochemically activated catalyst (EA-CA-CuSe), initially composed of Cu_2O nanocubes, achieves 82% CO selectivity at a partial current density of 27.7 mA cm^{-2}. These findings not only corroborate previous observations on structural evolution in pure Cu catalysts but also extend them to Cu–Se systems, offering deeper insights into active phase formation.

Our results demonstrate that controlled pre-treatment and activation of $Cu_{2-x}Se$ pre-catalysts can steer the formation of desirable active sites, thereby guiding the rational design of efficient and selective copper-based electrocatalysts for CO_2 electroreduction and potentially other electrochemical transformations.

Author contributions

W. Hu prepared the samples and performed the electrochemical experiments, D. Balalta and T. Altantzis carried out the electron microscopy, J. Song and W. Hu did the XRD, Z. Chen and W. Hu performed the Raman characterization, I. Abbas, F. D'Acapito and D. Grandjean carried out the XAFS measurements and analysis. W. Hu and D. Balalta analyzed the STEM data. B. Barhács, M. Guba and T. Höltzl conducted the calculations. T. Höltzl, S. Bals, D. Grandjean, D. Pant and E. Janssens secured funding. D. Grandjean, D. Pant and E. Janssens directed the research project. W. Hu and D. Grandjean prepared the first version of the manuscript. All authors discussed the results and participated in writing the manuscript.

Conflicts of interest

There are no conflicts to declare.

Data availability

The data of this article are shown in the Figures and the ESI.† The data of the figures presenting experimental results are available on the KU Leuven's institutional research data repository at **https://rdr.kuleuven.be/dataverse/rdr** with **https://doi.org/10.48804/CYCRZD**. The cartesian coordinates of all calculated reaction intermediates can be found on Zenodo: **https://doi.org/10.5281/zenodo.12745044**.

Acknowledgements

This project has received funding from the European Union's Horizon 2020 MSCA-ITN programme under grant agreement no. 955650 (CATCHY) and by the Moonshot program of Catalisti and VLAIO (Flanders Innovation & Entrepreneurship) under grant number HBC.2021.0586 (CLUE). T. H. is grateful for the János Bolyai Research Scholarship of the Hungarian Academy of Sciences (grant number BO/00642/21/7). B.B. is grateful to the University Research Scholarship Programme – Cooperative Doctoral Programme of the Hungarian National Research, Development and Innovation Office (grant number: EKÖP_KDP-24-1-BME-8) M.G. is grateful to the Cooperative Doctoral Programme for Doctoral Scholarships of the Hungarian National Research, Development and Innovation Office (KDP-23, grant number: C2273140). The authors are grateful to Zviadi Zarkua for his help with the XPS measurements and thank the ESRF for providing beamtime (CH-6247) and the staff of LISA-BM08 for their assistance.

References

1 B. Seger, M. Robert and F. Jiao, Best practices for electrochemical reduction of carbon dioxide, *Nat. Sustainability*, 2023, **6**, 236–238.
2 Y. Yang, S. Louisia, S. Yu, J. Jin, I. Roh, C. Chen, M. V. Fonseca Guzman, J. Feijóo, P. C. Chen, H. Wang, C. J. Pollock, X. Huang, Y. T. Shao, C. Wang, D. A. Muller, H. D. Abruña and P. Yang, Operando studies reveal active Cu nanograins for CO_2 electroreduction, *Nature*, 2023, **614**, 262–269.
3 Y. Wang, H. Shen, K. J. T. Livi, D. Raciti, H. Zong, J. Gregg, M. Onadeko, Y. Wan, A. Watson and C. Wang, Copper Nanocubes for CO_2 Reduction in Gas Diffusion Electrodes, *Nano Lett.*, 2019, **19**, 8461–8468.
4 K. Jiang, Y. Huang, G. Zeng, F. M. Toma, W. A. Goddard III and A. T Bell, Effects of Surface Roughness on the Electrochemical Reduction of CO_2 over Cu, *ACS Energy Lett.*, 2020, **5**, 1206–1214.
5 S. Mu, H. Lu, Q. Wu, L. Li, R. Zhao, C. Long and C. Cui, Hydroxyl radicals dominate reoxidation of oxide-derived Cu in electrochemical CO_2 reduction, *Nat. Commun.*, 2022, **13**, 3694.
6 H. Yang, Y. Wu, G. Li, Q. Lin, Q. Hu, Q. Zhang, J. Liu and C. He, Scalable Production of Efficient Single-Atom Copper Decorated Carbon Membranes for CO_2 Electroreduction to Methanol, *J. Am. Chem. Soc.*, 2019, **141**, 12717–12723.
7 D. Kim, J. Resasco, Y. Yu, A. M. Asiri and P. Yang, Synergistic geometric and electronic effects for electrochemical reduction of carbon dioxide using gold–copper bimetallic nanoparticles, *Nat. Commun.*, 2014, **5**, 4948.
8 X. Zhang, X. Sun, S.-X. Guo, A. M. Bond and J. Zhang, Formation of lattice-dislocated bismuth nanowires on copper foam for enhanced electrocatalytic CO_2 reduction at low overpotential, *Energy Environ. Sci.*, 2019, **12**, 1334–1340.
9 M. Wang, H. Chen, M. Wang, J. Wang, Y. Tuo, W. Li, S. Zhou, L. Kong, G. Liu, L. Jiang and G. Wang, Tuning C_1/C_2 Selectivity of CO_2 Electrochemical Reduction over in–Situ Evolved CuO/SnO_2 Heterostructure, *Angew. Chem., Int. Ed.*, 2023, **62**, e202306456.
10 W. Hu, D. Grandjean, J. Vaes, D. Pant and E. Janssens, Recent advances in copper chalcogenides for CO_2

electroreduction, *Phys. Chem. Chem. Phys.*, 2023, **25**, 30785.

11 D. Yang, Q. Zhu, C. Chen, H. Liu, Z. Liu, Z. Zhao, X. Zhang, S. Liu and B. Han, Selective electroreduction of carbon dioxide to methanol on copper selenide nanocatalysts, *Nat. Commun.*, 2019, **10**, 677.

12 L. Ding, N. Zhu, Y. Hu, Z. Chen, P. Song, T. Sheng, Z. Wu and Y. Xiong, Over 70% Faradaic Efficiency for CO_2 Electroreduction to Ethanol Enabled by K Dopant-Tuned Cu Sites-Intermediates Interaction, *Angew. Chem., Int. Ed.*, 2022, **61**, e202209268.

13 W. Sun, P. Wang, Y. Jiang, Z. Jiang, R. Long, Z. Chen, P. Song, T. Sheng, Z. Wu and Y. Xiong, V–Doped Cu_2Se Hierarchical Nanotubes Enabling Flow–Cell CO_2 Electroreduction to Ethanol with High Efficiency and Selectivity, *Adv. Mater.*, 2022, **34**, e2207691.

14 H. Wang, X. Bi, Y. Yan, Y. Zhao, Z. Yang, H. Ning and M. Wu, Efficient Electrocatalytic Reduction of CO_2 to Ethanol Enhanced by Spacing Effect of Cu-Cu in $Cu_{2-x}Se$ Nanosheets, *Adv. Funct. Mater.*, 2023, **33**, 2214946.

15 S. Li, J. Yu, S. Zhang, W. Qiu, X. Tang, Z. Lin, R. Cai, Y. Fang, S. Yang and X. Cai, Operando Reconstruction of Porous Carbon Supported Copper Selenide Promotes the C_2 Production from CO_2RR, *Adv. Funct. Mater.*, 2023, **34**, 2311989.

16 R. M. Arán-Ais, F. Scholten, S. Kunze, R. Rizo and B. Roldan Cuenya, The role of in situ generated morphological motifs and Cu(I) species in C_{2+} product selectivity during CO_2 pulsed electroreduction, *Nat. Energy*, 2020, **5**, 317–325.

17 C. Hahn, T. Hatsukade, Y.-G. Kim, A. Vailionis, J. H. Baricuatro, D. C. Higgins, S. A. Nitopi, M. P. Soriaga and T. F. Jaramillo, Engineering Cu surfaces for the electrocatalytic conversion of CO_2: Controlling selectivity toward oxygenates and hydrocarbons, *Proc. Natl. Acad. Sci. U. S. A.*, 2017, **114**, 5918–5923.

18 A. Eilert, F. Cavalca, F. S. Roberts, J. Osterwalder, C. Liu, M. Favaro, E. J. Crumlin, H. Ogasawara, D. Friebel, L. G. M. Pettersson and A. Nilsson, Subsurface oxygen in oxide-derived copper electrocatalysts for carbon dioxide reduction, *J. Phys. Chem. Lett.*, 2017, **8**, 285–290.

19 C. W. Li, J. Ciston and M. W. Kanan, Electroreduction of carbon monoxide to liquid fuel on oxide-derived nanocrystalline copper, *Nature*, 2014, **508**, 504–507.

20 K. W. Kimura, R. Casebolt, J. Cimada DaSilva, E. Kauffman, J. Kim, T. A. Dunbar, C. J. Pollock, J. Suntivich and T. Hanrath, Selective Electrochemical CO_2 Reduction during Pulsed Potential Stems from Dynamic Interface, *ACS Catal.*, 2020, **10**, 8632–8639.

21 C.-J. Chang, S.-C. Lin, H.-C. Chen, J. Wang, K. J. Zheng, Y. Zhu and H. M. Chen, Dynamic Reoxidation/Reduction-Driven Atomic Interdiffusion for Highly Selective CO_2 Reduction toward Methane, *J. Am. Chem. Soc.*, 2020, **142**, 12119–12132.

22 J. Li, F. Che, Y. Pang, C. Zou, J. Y. Howe, T. Burdyny, J. P. Edwards, Y. Wang, F. Li, Z. Wang, P. De Luna, C.-T. Dinh, T.-T. Zhuang, M. I. Saidaminov, S. Cheng, T. Wu, Y. Z. Finfrock, L. Ma, S.-H. Hsieh, Y.-S. Liu, G. A. Botton, W.-F. Pong, X. Du, J. Guo, T.-K. Sham, E. H. Sargent and D. Sinton, Copper adparticle enabled selective electrosynthesis of n-propanol, *Nat. Commun.*, 2018, **9**, 4614.

23 S. Yang, H. An, S. Arnouts, H. Wang, X. Yu, J. de Ruiter, S. Bals, T. Altantzis, B. M. Weckhuysen and W. van der Stam, Halide-guided active site exposure in bismuth electrocatalysts for selective CO_2 conversion into formic acid, *Nat. Catal.*, 2023, **6**, 796–806.

24 R. Amirbeigiarab, J. Tian, A. Herzog, C. Qiu, A. Bergmann, B. Roldan Cuenya and O. M. Magnussen, Atomic-scale surface restructuring of copper electrodes under CO_2 electroreduction conditions, *Nat. Catal.*, 2023, **6**, 837–846.

25 Y. Yuan, Q. Wang, Y. Qiao, X. Chen, Z. Yang, W. Lai, T. Chen, G. Zhang, H. Duan, M. Liu and H. Huang, In Situ Structural Reconstruction to Generate the Active Sites for CO_2 Electroreduction on Bismuth Ultrathin Nanosheets, *Adv. Energy Mater.*, 2022, **12**, 2200970.

26 Y. Jiang, X. Wang, D. Duan, C. He, J. Ma, W. Zhang, H. Liu, R. Long, Z. Li, T. Kong, X. J. Loh, L. Song, E. Ye and Y. Xiong, Structural Reconstruction of Cu_2O Superparticles toward Electrocatalytic CO_2 Reduction with High C_{2+} Products Selectivity, *Adv. Sci.*, 2022, **9**, 2105292.

27 W. Liu, P. Zhai, A. Li, B. Wei, K. Si, Y. Wei, X. Wang, G. Zhu, Q. Chen, X. Gu, R. Zhang, W. Zhou and Y. Gong, Electrochemical CO_2 reduction to ethylene by ultrathin CuO nanoplate arrays, *Nat. Commun.*, 2022, **13**, 1877.

28 B. Beverskog and I. Puigdomenech, Revised Pourbaix diagrams for copper at 25 to 300°C, *J. Electrochem. Soc.*, 1997, **144**, 3476.

29 S. Mu, H. Lu, Q. Wu, L. Li, R. Zhao, C. Long and C. Cui, Hydroxyl radicals dominate reoxidation of oxide-derived Cu in electrochemical CO_2 reduction, *Nat. Commun.*, 2022, **13**, 3694.

30 A. Yoon, J. Poon, P. Grosse, S. W. Chee and B. Roldan Cuenya, Iodide-mediated Cu catalyst restructuring during CO_2 electroreduction, *J. Mater. Chem. A*, 2022, **10**, 14041–14050.

31 R. Xiong, H. Xu, H. Zhu, Z. Zhang and G. Li, Recent progress in Cu-based electrocatalysts for CO_2 reduction, *Chem. Eng. J.*, 2025, **505**, 159210.

32 X. Li and X. Li, Promotion of Cu-Based Catalyst by Supported Ionic Liquid for Efficient Acetylene Hydrochlorination, *Mol. Catal.*, 2025, **584**, 115262.

33 R. Amirbeigiarab, J. Tian, A. Herzog, C. Qiu, A. Bergmann, B. Roldan Cuenya and O. M. Magnussen, Atomic-scale surface restructuring of copper electrodes under CO_2 electroreduction conditions, *Nat. Catal.*, 2023, **6**, 837–846.

34 Y. Zhu, H. Chen, C. Hsu, T. Lin, C. Chang, S. Chang, L. Tsai and H. Chen, Operando Unraveling of the Structural and Chemical Stability of P-Substituted $CoSe_2$ Electrocatalysts toward Hydrogen and Oxygen Evolution Reactions in Alkaline Electrolyte, *ACS Energy Lett.*, 2017, **4**, 987–994.

35 J. Xu, W. Zhang, Z. Yang, S. Ding, C. Zeng, L. Chen, Q. Wang and S. Yang, Large - Scale Synthesis of Long Crystalline $Cu_{2-x}Se$ Nanowire Bundles by Water–Evaporation–Induced Self–Assembly and Their Application in Gas Sensing, *Adv. Funct. Mater.*, 2009, **19**, 1759–1766.

36 S. A. Danilkin, A. N. Skomorokhov, A. Hoser, H. Fuess, V. Rajevac and N. N. Bickulova, Crystal structure and lattice dynamics of superionic copper selenide $Cu_{2-\delta}Se$, *J. Alloys Compd.*, 2003, **361**, 57–61.

37 M. C. Neuburger, Präzisionsmessung der Gitterkonstante von Cuprooxyd Cu_2O, *Z. Phys.*, 1931, **67**, 845–850.

38 H. Peng, J. Ren, Y. Wang, Y. Xiong, Q. Wang, Q. Li, X. Zhao, L. Zhan, L. Zheng, Y. Tang and Y. Lei, One-stone, two birds: Alloying effect and surface defects induced by Pt on $Cu_{2-x}Se$ nanowires to boost C-C bond cleavage for electrocatalytic ethanol oxidation, *Nano Energy*, 2021, **88**, 106307.

39 Y.-X. Zhang, T.-Y. Yang, Z.-H. Ge and J. Feng, High-performance copper selenide nanocomposites for power generation, *J. Eur. Ceram. Soc.*, 2023, **43**, 5255–5262.

40 T. H. Yin, B. J. Liu, Y. W. Lin, Y. S. Li, C. W. Lai, Y. P. Lan, C. Choi, H. C. Chang and Y. M. Choi, Electrodeposition of Copper Oxides as Cost-Effective Heterojunction Photoelectrode Materials for Solar Water Splitting, *Coatings*, 2022, **12**, 1839.

41 S. D. Sharma, K. Bayikadi, S. Raman and S. Neeleshwar, Structural, morphological and thermoelectric properties of self-decorated copper selenide nanosheets synthesized at room temperature, *Curr. Appl. Phys.*, 2022, **40**, 74–82.

42 W. Lee, N. Myung, K. Rajeshwar and C.-W. Lee, Electrodeposition of Cu_2Se Semiconductor Thin Film on Se-Modified Polycrystalline Au Electrode, *J. Electrochem. Sci. Technol.*, 2013, **4**, 140–145.

43 A. Abdalla, S. Bereznev, N. Spalatu, O. Volobujeva, N. Sleptsuk and M. Danilson, Pulsed laser deposition of Zn (O, Se) layers in nitrogen background pressure, *Sci. Rep.*, 2019, **9**, 17443.

44 G. D. Brabson, L. Andrews and C. J. Marsden, Reactions of Selenium and Oxygen. Matrix Infrared Spectra and Density Functional Calculations of Novel Se_xO_y Molecules, *J. Phys. Chem.*, 1996, **100**, 16487–16494.

45 J. Huang, N. Hörmann, E. Oveisi, A. Loiudice, G. Luca De Gregorio, O. Andreussi, N. Marzari and R. Buonsanti, Potential-induced nanoclustering of metallic catalysts during electrochemical CO_2 reduction, *Nat. Commun.*, 2018, **9**, 3117.

46 M. Bernal, A. Bagger, F. Scholten, I. Sinev, A. Bergmann, M. Ahmadi, J. Rossmeisl and B. Roldan Cuenya, CO_2 electroreduction on copper-cobalt nanoparticles: Size and composition effect, *Nano Energy*, 2018, **53**, 27–36.

47 A. Yoon, J. Poon, P. Grosse, S. W. Chee and B. Roldan Cuenya, Iodide-mediated Cu catalyst restructuring during CO_2 electroreduction, *J. Mater. Chem. A*, 2022, **10**, 14041–14050.

48 Q. Ren, N. Zhang, Z. Dong, L. Zhang, X. Chen and L. Luo, Structural evolution of Cu_2O nanocube electrocatalysts for the CO_2 reduction reaction, *Nano Energy*, 2023, **106**, 108080.

49 P. Grosse, A. Yoon, C. Rettenmaier, A. Herzog, S. W. Chee and B. Roldan Cuenya, Dynamic transformation of cubic copper catalysts during CO_2 electroreduction and its impact on catalytic selectivity, *Nat. Commun.*, 2021, **12**, 6736.

50 W. J. Durand, A. A. Peterson, F. Studt, F. Abild-Pedersen and J. K. Nørskov, Structure effects on the energetics of the electrochemical reduction of CO_2 by copper surfaces, *Surf. Sci.*, 2011, **605**, 1354–1359.

51 O. J. Wahab, M. Kang, E. Daviddi, M. Walker and P. R. Unwin, Screening Surface Structure–Electrochemical Activity Relationships of Copper Electrodes under CO_2 Electroreduction Conditions, *ACS Catal.*, 2022, **12**, 6578–6588.

52 T. Yang, T. Gu, Y. Han, W. Wang, Y. Yu, Y. Zang, H. Zhang, B. Mao, Y. Li, B. Yang and Z. Liu, Surface Orientation and Pressure Dependence of CO_2 Activation on Cu Surfaces, *J. Phys. Chem. C*, 2020, **124**, 27511–27518.

53 A. A. Peterson, F. Abild-Pedersen, F. Studt, J. Rossmeisl and J. K. Nørskov, How copper catalyzes the electroreduction of carbon dioxide into hydrocarbon fuels, *Energy Environ. Sci.*, 2010, **3**, 1311–1315.

54 J. Hussain, H. Jónsson and E. Skúlason, Calculations of Product Selectivity in Electrochemical CO_2 Reduction, *ACS Catal.*, 2018, **8**, 5240–5249.